

Biglobal Stability of Cylindrically-Shaped Hybrid and Solid Rockets with Injecting or Reactive Headwalls

Trevor S. Elliott,^{*} Joshua W. Batterson,[†] and Joseph Majdalani[‡]
University of Tennessee Space Institute, Tullahoma, TN 37388, USA

The purpose of this study is to investigate the biglobal stability of a simulated rocket chamber with a cylindrical grain perforation and a variable headwall injection. Our effort is motivated by the need to characterize the hydrodynamic stability of the flowfield that evolves in both cylindrically-shaped hybrid and solid rocket motors with reactive headwalls. To this end, the biglobal stability approach is applied to the incompressible Navier-Stokes equations, which can be resolved while assuming Berman's self-similar half-cosine profile at the chamber headwall. The corresponding headwall injection constant is thus varied from 0.5 in the case of solid rocket motors to 50 in the case of hybrid rocket engines. The present analysis constitutes a natural extension to previous stability investigations that rely on either one-dimensional Local Nonparallel (LNP) formulations with headwall injection or on strictly two-dimensional biglobal stability formulations based on an axisymmetric stream function representation and no headwall injection. Here, we do not limit ourselves to a stream function formulation but rather consider the complete Navier-Stokes equations in the context of a biglobal stability framework. The resulting linearized eigenproblem is solved using pseudo-spectral methods and a judicious set of boundary conditions that are consistent with either hybrid or solid rocket chambers. At the outset, the stability spectrum for a solid rocket motor with an inert headwall is recovered as a special case. Finally, a comparison to previous work that employs the LNP approach is provided and discussed.

Nomenclature

A_{ij}	= operator matrix
a	= chamber radius
B_{ij}	= the right-hand-side coefficient matrix of a matrix pencil
D_N	= Chebyshev pseudo-spectral derivative matrix of size N
d	= weight coefficients for pseudo-spectral derivative matrices
I_N	= identity matrix of size N
L	= chamber length
M	= base flow component
\tilde{M}	= instantaneous flow component
m	= general amplitude function
\hat{m}	= acoustic fluctuation
\tilde{m}	= unsteady hydrodynamic fluctuation
$\tilde{\tilde{m}}$	= vortical fluctuation
\mathcal{O}	= Landau order symbol
P	= base flow pressure
p	= pressure amplitude function
\tilde{p}	= hydrodynamic pressure fluctuation
q	= azimuthal integer wave number
r	= normalized radial coordinate

^{*}Graduate Research Assistant, Department of Mechanical, Aerospace and Biomedical Engineering. Member AIAA.

[†]Adjunct Assistant Professor, Department of Mechanical, Aerospace and Biomedical Engineering. Member AIAA.

[‡]H. H. Arnold Chair of Excellence in Advanced Propulsion, Department of Mechanical, Aerospace and Biomedical Engineering. Associate Fellow AIAA. Fellow ASME.

Re	= Reynolds number
T_N	= Chebyshev polynomial of the first kind
\mathbf{U}	= base flow velocity, U_r, U_θ, U_z
u	= velocity amplitude function
\tilde{u}	= hydrodynamic velocity fluctuation
z	= normalized axial coordinate

Greek

∇	= gradient operator
ε	= $1/Re$
η	= streamwise Chebyshev variables mapped between [-1, 1]
λ	= eigenvalue
ω	= complex frequency of oscillations, $\omega_r + i\omega_i$
ω_i	= temporal stability growth rate
ω_r	= dimensionless circular frequency
θ	= tangential coordinate
ξ	= radial Chebyshev variables mapped between [-1, 1]

Subscripts and Superscripts

i	= denotes an imaginary component
ii	= diagonal matrix or diagonal element
ij	= matrix or matrix elements
h	= property at the headwall
N	= Chebyshev polynomial order/number of collocation points
r	= denotes a real component
w	= property at the sidewall
n	= denotes the order of the derivative

I. Introduction

HYDRODYNAMIC stability investigations of rocket chambers may be traced back to the pioneering work of Varapaev and Yagodkin,¹ and to those connected with turbulence characterization in simulated rocket configurations, such as Beddini,² Beddini and Roberts,³ Lee and Beddini,^{4,5} Apte and Yang,⁶⁻⁸ Wasistho, Balachandar and Moser,⁹ and others. Along similar lines, several research studies by Casalis and co-workers, especially those by Casalis, Avalon, and Pineau,¹⁰ Griffond, Casalis and Pineau,¹¹ Ugurtas *et al.*,¹² Griffond and Casalis,^{13,14} Féraille and Casalis,¹⁵ and Fabignon *et al.*¹⁶ pay special attention to different hydrodynamic stability models and their ability to predict with varying degrees of accuracy the oscillatory motions observed in solid rocket boosters such as Ariane. Among their achievements, these studies help to identify some of the sources of instability, such as parietal, obstacle, and angle vortex shedding, clarify the connection between the stability eigenmodes and the reported frequencies, delineate the salient acoustic frequencies and pressure shifts, and shed some light on the basic inconsistencies between techniques that entail perturbations of the primitive variables, and those that rely on stream function formulations.²⁻⁵ They also help to explain the spatial evolution of disturbances in simulated porous channels and tubes, which mimic the flowfield in solid rocket motors. From a practical perspective, the theoretical findings obtained through hydrodynamic stability models are not only supported by lab-scale firings,¹⁷ they are further corroborated by cold-flow data acquired using two elegantly designed experimental facilities coined VECLA (*Veine d'Etude de la Couche Limite Acoustique*) and VALDO (*Veine Axisymétrique pour Limiter le Développement des Oscillations*). These two facilities are associated with two-dimensional, planar and axisymmetric flow investigations, respectively (see Avalon, Casalis and Pineau¹⁸). Other essential wave characteristics are elucidated through the work of Avalon and Comas,¹⁹ Vuillot and Avalon;²⁰ Vuillot,²¹ Couton *et al.*,²² and Ugurtas *et al.*²³

In what concerns the stability of solid rocket motors, the most noteworthy developments, perhaps, may be associated with the adoption of a biglobal framework by Chedevergne and Casalis,^{24,25} specifically in a compelling stream function formulation that brings about new insights into the unresolved thrust oscillation problem. The same study winds up earning the 2007 AIAA Best Solid Rocket Paper Award. This particular effort is accompanied by

two sequels attributed to Chedevergne, Casalis, and Féraille,²⁶ and Chedevergne, Casalis, and Majdalani.²⁷ In the last installment, direct numerical simulations of cylindrically-perforated solid rocket motor grains are shown to coincide quite closely with biglobal stability predictions of the ensuing unsteady motion when properly augmented by the vorticoacoustic wave contribution formulated by Majdalani and Van Moorhem.²⁸

In the realm of liquid rocket flowfield stability, the first serious investigation of note may be attributed to Batterson and Majdalani^{29,30} and their biglobal stability analysis of the bidirectional vortex motion that arises in the context of the so-called Vortex Combustion Cold Wall Chamber (VCCWC) by Chiaverini *et al.*³¹⁻³⁴ This two-part series provides, first and foremost, the detailed analytical derivation, numerical discretization steps, and spectral collocation tools needed to handle the complete set of partial differential equations that emerge in a problem where the parallel flow assumption is relaxed. Second, it illustrates the practical application of biglobal stability to the incompressible helical profiles associated with the VCCWC configuration. It thus manages in providing the stability eigensolutions for the complex lamellar,^{35,36} linear,³⁷ and nonlinear Beltramian motions,³⁸ using a realistic set of boundary conditions associated with choked chamber conditions. Among its main outcomes, the Batterson-Majdalani study shows that the stability of helical motions can be substantially enhanced by increasing swirl while securing an axisymmetric flow configuration throughout the chamber. In the case of unstable modes, which can occur for low values of swirl, their manifestation is found to be most pronounced near the headwall, namely, in the funnel region where flow turning and shearing are most appreciable. Everywhere else, the disturbances are seen to faithfully follow the paths prescribed by the mean flow streamlines.

As far as hybrid flowfield analysis is concerned, the application of hydrodynamic instability theory in the context of a simulated hybrid rocket engine may be ascribed to the work of Abu-Irshaid, Majdalani, and Casalis.³⁹ In this investigation, the one-dimensional, LNP approach is evoked to analyze the stability of a hybrid rocket chamber that admits a half-cosine injection pattern at its headwall. The study itself focuses on the effects of headwall injection on the stability of the extended Taylor-Culick profile, which is described in detail by Majdalani,⁴⁰ and Majdalani and Akiki.⁴¹ Using $u_h = U_0 / (\pi U_w)$ as a measure of the relative intensity of headwall-to-sidewall injection, the LNP model shows that increasing u_h leads to a shift in the neutral curve upstream of the headwall. It also suggests that further increases in u_h result in unstable behavior over a progressively expanding range of frequencies throughout the chamber. The analogous case of a solid rocket motor with a reactive headwall is accompanied by a narrower instability band. In short, these findings indicate that, when all conditions are set equal, a hybrid rocket flowfield will be intrinsically less stable than that of a solid rocket motor.

At this point it may be instructive to note that the spatial stability study employed by Abu-Irshaid, Majdalani, and Casalis³⁹ requires selection of a certain azimuthal integer wave number q and frequency $\omega = \omega_r$. Naturally, its imaginary frequency is suppressed, i.e. $\omega_i = 0$, in accordance with the spatial stability approach. The LNP method determines at each spatial position, the spatial growth rate ($-\alpha_i$) and the longitudinal wave number α_r for given values of the operating Reynolds number and headwall injection constant. In the present work, we shift from the one-dimensional LNP approach to the biglobal framework outlined by Batterson and Majdalani.²⁹ In this vein, the specification of the azimuthal wave number will be necessary to determine the entire stability spectrum for a given Reynolds number and u_h . The temporal stability analysis of Chedevergne, Casalis, and Féraille²⁶ is somewhat similar except for its reliance on a single value of $q=0$ and the Arnoldi algorithm to compute a specific number of eigenvalues near a starting point. In the present work, the QZ algorithm will be used instead to determine the eigenmodes for the first four azimuthal wave numbers in both hybrid rocket chambers and solid rocket motors having non-inert headwalls.

The paper is organized as follows: In Sec. II, we introduce the problem configuration consisting of the physical geometry and flowfields under investigation. We then layout the hydrodynamic stability theory along with the fundamental biglobal stability equations in Sec. III, following the work of Batterson and Majdalani.^{29,30} Then, in Sec. IV, the Chebyshev collocation method is selected and discussed in view of its direct relevance to our problem. In this section, the spectral equations are formulated from the general eigenvalue problem and the boundary conditions associated with the flow under investigation are defined. Finally, in Sec. V, numerical results for each core flowfield are presented and discussed, with a summary that is given in Sec. VI.

II. Problem Configuration

In this study we consider a motor case with a cylindrical grain perforation. The corresponding hybrid and solid rocket core flowfields are depicted schematically in Figure 1a,b where the motor is represented as a cylindrical chamber of length L and radius a . The headwall injection velocity is assumed to be Berman's cosine function with

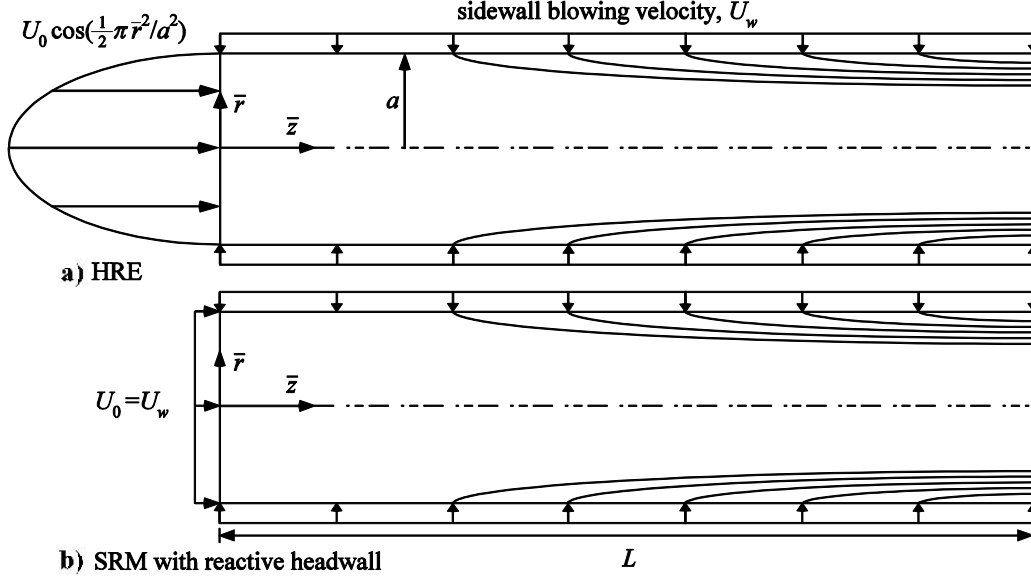


Figure 1. Geometric sketches of a) internal burning hybrid grain with cylindrical perforation and sinusoidally imposed headwall injection, and b) simulated solid rocket motor with equally injecting headwall and sidewall.

a maximum centerline velocity equal to U_0 . In order to reproduce the rate of mass addition at the injector faceplate of a hybrid rocket, the headwall injection velocity may be varied. Additionally, the independent sidewall injection, U_w , may be calibrated to capture the regression rate of the fuel grain in the case of a hybrid, or the solid propellant in the case of a solid rocket motor. As implied in our Nomenclature, all coordinates are normalized by the chamber radius and all velocities are normalized by U_w :

$$U_r = \frac{\bar{U}_r}{U_w}; U_\theta = \frac{\bar{U}_\theta}{U_w}; U_z = \frac{\bar{U}_z}{U_w}; r = \frac{\bar{r}}{a}; z = \frac{\bar{z}}{a} \quad (1)$$

Furthermore, the headwall injection constant, u_h , is defined as

$$u_h = U_0 / (\pi U_w) \quad (2)$$

According to Majdalani,⁴⁰ the mean flow components may be expressed as

$$U_r = -\frac{1}{r} \sin(\frac{1}{2} \pi r^2); U_z = \pi(z + u_h) \cos(\frac{1}{2} \pi r^2); U_\theta = 0 \quad (3)$$

It should be pointed out that $z=0$ stands for the upstream edge of the porous wall and that the headwall injection constant germane to hybrid rockets can vary in the range of $50 \leq u_h \leq 500$, with a typical value of 50. For a solid rocket motor (SRM), one may assume that the same propellant is present at both the sidewall, where the injection is uniform, and the headwall, where the profile is cosine-shaped. This arrangement leads to a value of $u_h = \frac{1}{2}$. The resulting idealization ensures that the headwall mass injection rate is equal to $\rho \pi a^2 U_w$, thus making the model consistent with that of a sufficiently long grain, which burns equally uniformly along its sidewall and headwall, as in depicted in Figure 1b.

III. Biglobal Hydrodynamic Stability Theory

The instantaneous velocity may be considered to be the sum of a steady part and three fluctuating wave disturbances,

$$\tilde{M} = M + \hat{m} + \tilde{m} + \bar{m} \quad (4)$$

Here \tilde{M} denotes the instantaneous flowfield and M refers to the base flow. The next two terms represent the compressible, irrotational acoustic wave, \hat{m} , and the rotational, incompressible vortical wave, \tilde{m} . The combination of these two components constitutes what has become known as the vorticoacoustic wave, a time-dependent motion that is adequately modeled by Majdalani and co-workers in a variety of physical settings.^{28,42-46} The last term corresponds to the hydrodynamic instability wave, \bar{m} , which, unlike its vorticoacoustic counterpart, evolves over a wide spectrum of frequencies and length scales. For this reason, spectral methods may be best suited to discern its character.

Because the vorticoacoustic contribution is well known, our attention will remain concentrated on the hydrodynamic instability contribution. We therefore begin our analysis by superimposing the base flow to the hydrodynamic wave, which appears as a first-order perturbation,

$$\tilde{M} = M + \tilde{m} \quad (5)$$

Applying this perturbation expansion to the viscous, incompressible Navier-Stokes equations leads to a set of Linearized Navier-Stokes (LNS) equations. As shown by Batterson and Majdalani,²⁹ we get

Continuity:

$$\frac{\partial \tilde{u}_r}{\partial r} + \frac{\tilde{u}_r}{r} + \frac{1}{r} \frac{\partial \tilde{u}_\theta}{\partial \theta} + \frac{\partial \tilde{u}_z}{\partial z} = 0 \quad (6)$$

Radial momentum:

$$\begin{aligned} \frac{\partial \tilde{u}_r}{\partial t} + U_r \frac{\partial \tilde{u}_r}{\partial r} + \tilde{u}_r \frac{\partial U_r}{\partial r} + \frac{U_\theta}{r} \frac{\partial \tilde{u}_\theta}{\partial \theta} + \frac{\tilde{u}_\theta}{r} \frac{\partial U_r}{\partial \theta} - \frac{2U_\theta \tilde{u}_\theta}{r} + U_z \frac{\partial \tilde{u}_r}{\partial z} + \tilde{u}_z \frac{\partial U_r}{\partial z} + \frac{\partial \tilde{p}}{\partial r} \\ = \varepsilon \left(\frac{\partial^2 \tilde{u}_r}{\partial r^2} + \frac{1}{r} \frac{\partial \tilde{u}_r}{\partial r} - \frac{\tilde{u}_r}{r^2} + \frac{1}{r^2} \frac{\partial^2 \tilde{u}_r}{\partial \theta^2} - \frac{2}{r^2} \frac{\partial \tilde{u}_\theta}{\partial \theta} + \frac{\partial^2 \tilde{u}_r}{\partial z^2} \right) \end{aligned} \quad (7)$$

Tangential momentum:

$$\begin{aligned} \frac{\partial \tilde{u}_\theta}{\partial t} + U_r \frac{\partial \tilde{u}_\theta}{\partial r} + \tilde{u}_r \frac{\partial U_\theta}{\partial r} + \frac{U_\theta}{r} \frac{\partial \tilde{u}_\theta}{\partial \theta} + \frac{\tilde{u}_\theta}{r} \frac{\partial U_\theta}{\partial \theta} + \frac{U_r \tilde{u}_\theta}{r} + \frac{\tilde{u}_r U_\theta}{r} + U_z \frac{\partial \tilde{u}_\theta}{\partial z} + \tilde{u}_z \frac{\partial U_\theta}{\partial z} + \frac{1}{r} \frac{\partial \tilde{p}}{\partial \theta} \\ = \varepsilon \left(\frac{\partial^2 \tilde{u}_\theta}{\partial r^2} + \frac{1}{r} \frac{\partial \tilde{u}_\theta}{\partial r} - \frac{\tilde{u}_\theta}{r^2} + \frac{1}{r^2} \frac{\partial^2 \tilde{u}_\theta}{\partial \theta^2} + \frac{2}{r^2} \frac{\partial \tilde{u}_r}{\partial \theta} + \frac{\partial^2 \tilde{u}_\theta}{\partial z^2} \right) \end{aligned} \quad (8)$$

Axial momentum:

$$\frac{\partial \tilde{u}_z}{\partial t} + U_r \frac{\partial \tilde{u}_z}{\partial r} + \tilde{u}_r \frac{\partial U_z}{\partial r} + \frac{U_\theta}{r} \frac{\partial \tilde{u}_z}{\partial \theta} + \frac{\tilde{u}_\theta}{r} \frac{\partial U_z}{\partial \theta} + U_z \frac{\partial \tilde{u}_z}{\partial z} + \tilde{u}_z \frac{\partial U_z}{\partial z} + \frac{\partial \tilde{p}}{\partial z} = \varepsilon \left(\frac{\partial^2 \tilde{u}_z}{\partial r^2} + \frac{1}{r} \frac{\partial \tilde{u}_z}{\partial r} + \frac{1}{r^2} \frac{\partial^2 \tilde{u}_z}{\partial \theta^2} + \frac{\partial^2 \tilde{u}_z}{\partial z^2} \right) \quad (9)$$

where the collection of terms at $\mathcal{O}(M)$ may be dropped, being identically satisfied by the mean flowfield associated with Eq. (3). Furthermore, second-order terms of $\mathcal{O}(\tilde{m}^2)$ and higher may be truncated in the process of identifying the first-order stability equations.

Equations (6)-(9) may be further reduced by assuming a biglobal modal ansatz of the form

$$\tilde{m} = m(r, z) \exp[i(q\theta - \omega t)] \quad (10)$$

This ansatz only requires that the base flow be periodic with respect to θ . The two-dimensional amplitude function, $m(r, z)$, enables us to globally compute the spatial waveform. Substitution of this ansatz gives rise to the following biglobal stability equations:

Continuity:

$$\left(\frac{\partial}{\partial r} + r^{-1} \right) u_r + (iqr^{-1}) u_\theta + \left(\frac{\partial}{\partial z} \right) u_z = 0 \quad (11)$$

Radial momentum:

$$\begin{aligned} \left\{ \frac{\partial \tilde{u}_r}{\partial t} + U_r \frac{\partial}{\partial r} + \frac{\partial U_r}{\partial r} + iqU_\theta r^{-1} + U_z \frac{\partial}{\partial z} - \varepsilon \left[\frac{\partial^2}{\partial r^2} + r^{-1} \frac{\partial}{\partial r} - (1+q^2)r^{-2} + \frac{\partial^2}{\partial z^2} \right] \right\} u_r \\ + \left(2iq\varepsilon r^{-2} - 2U_\theta r^{-1} + r^{-1} \frac{\partial U_r}{\partial \theta} \right) u_\theta + \left(\frac{\partial U_r}{\partial z} \right) u_z + \left(\frac{\partial}{\partial r} \right) p = (i\omega) u_r \end{aligned} \quad (12)$$

Tangential momentum:

$$\begin{aligned} \left(\frac{\partial U_\theta}{\partial r} + U_\theta r^{-1} - 2iq\varepsilon r^{-2} \right) u_r + \left\{ U_r \frac{\partial}{\partial r} + U_r r^{-1} + iqU_\theta r^{-1} + r^{-1} \frac{\partial U_\theta}{\partial \theta} + U_z \frac{\partial}{\partial z} \right. \\ \left. - \varepsilon \left[\frac{\partial^2}{\partial r^2} + r^{-1} \frac{\partial}{\partial r} - (1+q^2)r^{-2} + \frac{\partial^2}{\partial z^2} \right] \right\} u_\theta + \left(\frac{\partial U_\theta}{\partial z} \right) u_z + (iqr^{-1}) p = (i\omega) u_\theta \end{aligned} \quad (13)$$

Axial momentum:

$$\left(\frac{\partial U_z}{\partial r} \right) u_r + \left(r^{-1} \frac{\partial U_z}{\partial \theta} \right) u_z + \left[U_r \frac{\partial}{\partial r} + iqU_\theta r^{-1} + \frac{\partial U_z}{\partial z} + U_z \frac{\partial}{\partial z} \right]$$

$$-\varepsilon \left(\frac{\partial^2}{\partial r^2} + r^{-1} \frac{\partial}{\partial r} - q^2 r^{-2} + \frac{\partial^2}{\partial z^2} \right) u_z + \left(\frac{\partial}{\partial z} \right) p = (i\omega) u_z \quad (14)$$

In previous work, a similar set of biglobal stability equations are developed by Robitaille-Montané and Casalis,⁴⁷ albeit in Cartesian coordinates.

IV. Chebyshev Discretization

A Chebyshev collocation stencil is selected over other discretization methods due to its simplicity and straightforward application. We define a discrete Chebyshev polynomial of order N as

$$P_N f(\xi) = \sum_{i=1}^N f(\xi_i) \lambda_i(\xi) \quad (15)$$

In the above, ξ_i represents the collocation point corresponding to $i=1, \dots, N$ whereas $\lambda_i(\xi)$ stands for the appropriate weight function. For Chebyshev polynomials, we have

$$\lambda_i(\xi) = (-1)^i \left(\frac{1-\xi^2}{\xi-\xi_i} \right) \left[\frac{T'_{N-1}(\theta)}{d_i(N-1)^2} \right] \quad \text{with} \quad \begin{cases} \xi_i = \cos \left[\frac{(i-1)\pi}{N-1} \right] \\ \theta = \arccos \xi \end{cases} \quad (16)$$

where

$$d_i = \begin{cases} 2; & i = 1 \text{ or } N \\ 1; & \text{otherwise} \end{cases} \quad (17)$$

This polynomial structure can be employed to generate a discretization scheme such as the Chebyshev pseudo-spectral differentiation matrix defined below.^{48,49}

A. Chebyshev Differentiation Matrix

For each $N \geq 1$, one can let the rows and columns of the $(N+1) \times (N+1)$ Chebyshev spectral differentiation matrix D_N be indexed from 0 to N . The entries of the matrix are:²⁹

$$D_N = \begin{cases} (D_N)_{11} = \frac{2(N-1)^2 + 1}{6}; & (D_N)_{ii} = \frac{-\xi_i}{2(1-\xi_i^2)} \quad i = 2, \dots, N-1 \\ (D_N)_{ij} = \frac{d_i (-1)^{i+j}}{d_j (\xi_i - \xi_j)} & i \neq j, \quad i, j = 2, \dots, N-1 \\ (D_N)_{NN} = -\frac{2(N-1)^2 + 1}{6} \end{cases} \quad (18)$$

Higher order derivatives can be computed by simply raising the first order pseudo-spectral differentiation matrix to the corresponding power. For example, one may take:

$$\frac{d^n}{d\xi^n} \rightarrow (D_N)^n = \underbrace{D_N \times D_N \times \dots \times D_N}_{\times n} \quad (19)$$

The axisymmetric problem now requires a two-dimensional grid based on directionally independent Chebyshev points, or a tensor product grid.⁵⁰ This grid allows two independent variables to appear in the same matrix operator. For this reason, Kronecker products are required for tensor product grids. Using standard notation, the Kronecker product of two matrices is denoted by $A_{ij} \otimes B_{mn} = C_{ixm jxn}$ where $C_{ixm jxn}$ represents a block matrix such that each block is built according to $a_{ij} B_{mn}$. The Kronecker product can be applied to the differentiation matrix to specify derivatives in two directions. In what follows, derivatives with respect to η will be taken as $(I_N) \otimes (D_N)^n$ while derivatives with respect to ξ will be written as $(D_N)^n \otimes (I_N)$, where (I_N) stands for the $N \times N$ identity matrix. Both η and ξ are defined next.

B. Principal Matrices

As we are interested in the spectral decomposition and eigensolution to this problem, our system is formulated in terms of the generalized eigenvalue problem,

$$A_{ij}f_i = \lambda B_{ij}f_i \quad (20)$$

The solution domain must be transformed for the r and z independent coordinates. The two-dimensional mapping formula for arbitrary chamber length Z_N over the domain $0 \leq r \leq 1$ and $0 \leq z \leq Z_N$ may be reconditioned using

$$\begin{cases} r = \frac{1}{2}(\xi + 1) & \text{or} & \xi = 2r - 1 \\ z = \frac{Z_N}{2}(\eta + 1) & \text{or} & \eta = \frac{2z - Z_N}{Z_N} \end{cases} \begin{cases} \frac{\partial}{\partial r} = 2 \frac{\partial}{\partial \xi} \\ \frac{\partial}{\partial z} = \frac{2}{Z_N} \frac{\partial}{\partial \eta} \end{cases} \quad (21)$$

The corresponding block matrices take on the form:

$$\begin{cases} A_{c,u_r} = \bar{D}_N^r + r_{ii}^{-1} \\ A_{c,u_\theta} = iq r_{ii}^{-1} \\ A_{c,u_z} = \bar{D}_N^z \\ A_{c,p} = 0 \end{cases} \begin{cases} B_{c,u_r} = 0 \\ B_{c,u_\theta} = 0 \\ B_{c,u_z} = 0 \\ B_{c,p} = 0 \end{cases} \quad (\text{continuity}) \quad (22)$$

$$\begin{cases} A_{r,u_r} = U_{r,ii} \bar{D}_N^r + \left(\frac{\partial U_r}{\partial r} \right)_{ii} + iq U_{\theta,ii} r_{ii}^{-1} + U_{z,ii} \bar{D}_N^z \\ \quad - \varepsilon \left[(\bar{D}_N^r)^2 + r_{ii}^{-1} \bar{D}_N^r - (1 - q^2) r_{ii}^{-2} + (\bar{D}_N^z)^2 \right] \\ A_{r,u_\theta} = 2iq \varepsilon r_{ii}^{-2} - 2U_{\theta,ii} r_{ii}^{-1} + r_{ii}^{-1} \left(\frac{\partial U_r}{\partial \theta} \right)_{ii} \\ A_{r,u_z} = \left(\frac{\partial U_r}{\partial z} \right)_{ii} \\ A_{r,p} = \bar{D}_N^r \end{cases} \begin{cases} B_{r,u_r} = iI_N \\ B_{r,u_\theta} = 0 \\ B_{r,u_z} = 0 \\ B_{r,p} = 0 \end{cases} \quad (\text{radial momentum}) \quad (23)$$

$$\begin{cases} A_{\theta,u_r} = \left(\frac{\partial U_\theta}{\partial r} \right)_{ii} + U_{\theta,ii} r_{ii}^{-1} - 2iq \varepsilon r_{ii}^{-2} \\ A_{\theta,u_\theta} = U_{r,ii} \bar{D}_N^r + r_{ii}^{-1} \left(\frac{\partial U_\theta}{\partial \theta} \right)_{ii} + iq U_{\theta,ii} r_{ii}^{-1} + U_{z,ii} \bar{D}_N^z \\ \quad U_{r,ii} r_{ii}^{-1} - \varepsilon \left[(\bar{D}_N^r)^2 + r_{ii}^{-1} \bar{D}_N^r - (1 + q^2) r_{ii}^{-2} + (\bar{D}_N^z)^2 \right] \\ A_{\theta,u_z} = \left(\frac{\partial U_\theta}{\partial z} \right)_{ii} \\ A_{\theta,p} = iq r_{ii}^{-1} \end{cases} \begin{cases} B_{\theta,u_r} = 0 \\ B_{\theta,u_\theta} = iI_N \\ B_{\theta,u_z} = 0 \\ B_{\theta,p} = 0 \end{cases} \quad (\text{tangential}) \quad (24)$$

$$\begin{cases} A_{z,u_r} = \left(\frac{\partial U_z}{\partial r} \right)_{ii} \\ A_{z,u_\theta} = r_{ii}^{-1} \left(\frac{\partial U_z}{\partial \theta} \right)_{ii} \\ A_{z,u_z} = U_{r,ii} \bar{D}_N^r + \left(\frac{\partial U_z}{\partial z} \right)_{ii} + iq U_{\theta,ii} r_{ii}^{-1} + U_{z,ii} \bar{D}_N^z \\ \quad - \varepsilon \left[(\bar{D}_N^r)^2 + r_{ii}^{-1} \bar{D}_N^r - q^2 r_{ii}^{-2} + \bar{D}_N^z \right] \\ A_{z,p} = \bar{D}_N^z \end{cases} \begin{cases} B_{z,u_r} = 0 \\ B_{z,u_\theta} = 0 \\ B_{z,u_z} = iI_N \\ B_{z,p} = 0 \end{cases} \quad (\text{axial}) \quad (25)$$

where the overbar is used as a reminder that the spectral operators are mapped to the physical domain.

C. Boundary Conditions

Having defined the operating matrices, one is left with the need to specify a judicious set of auxiliary conditions. The physical requirements at the chamber boundaries and centerline may be taken to realistically correspond to the acoustic field in a circular tube with acoustically closed endpoints, i.e. $\mathbf{n} \cdot \mathbf{u} = 0$ and $\mathbf{n} \cdot \nabla p = 0$. Finally, closure for an axisymmetric system may be achieved by letting

$$\begin{cases} u_r(0, z) = 0 \\ u_r(1, z) = 0 \\ u_r(r, 0) = 0 \\ u_r(r, Z_N) = 0 \end{cases} \begin{cases} u_\theta(0, z) = 0 \\ u_\theta(1, z) = 0 \\ u_\theta(r, 0) = 0 \\ u_\theta(r, Z_N) = 0 \end{cases} \begin{cases} \partial_r u_z(0, z) = 0 \\ u_z(1, z) = 0 \\ u_z(r, 0) = 0 \\ u_z(r, Z_N) = 0 \end{cases} \begin{cases} \partial_r p(0, z) = 0 \\ \partial_r p(1, z) = 0 \\ \partial_z p(r, 0) = 0 \\ \partial_z p(r, Z_N) = 0 \end{cases} \quad (26)$$

Note that the streamwise conditions on all velocities at the headwall are suppressed in order to satisfy the no-slip requirement. Similarly, the velocity and pressure boundary conditions at the downstream section are selected to conform with an acoustically closed chamber. According to one-dimensional local theory, spatial instability is first observed in axisymmetric modes, a scenario that renders the analysis of higher modes inconsequential. This is confirmed by Abu-Irshaid, Majdalani, and Casalis,³⁹ whose iso- n plots display the growth rate n connecting the abscissa of spatial instability with temporal theory. However, traverse mode instability, which is particularly relevant in liquid rockets with headwall injection, more commonly occurs in asymmetric modes. Assuming that analogous modes may occur in cylindrically-shaped hybrid rocket engines, the case of $|q| > 0$ will also be considered by modifying the centerline boundary conditions to the extent of representing axisymmetric motion. The asymmetric analog of Eq. (26) becomes

$$\begin{cases} u_r(0, z) = 0 \\ u_r(1, z) = 0 \\ u_r(r, 0) = 0 \\ u_r(r, Z_N) = 0 \end{cases} \begin{cases} u_\theta(0, z) = 0 \\ u_\theta(1, z) = 0 \\ u_\theta(r, 0) = 0 \\ u_\theta(r, Z_N) = 0 \end{cases} \begin{cases} u_z(0, z) = 0 \\ u_z(1, z) = 0 \\ u_z(r, 0) = 0 \\ u_z(r, Z_N) = 0 \end{cases} \begin{cases} p(0, z) = 0 \\ \partial_r p(1, z) = 0 \\ \partial_z p(r, 0) = 0 \\ \partial_z p(r, Z_N) = 0 \end{cases} \quad (27)$$

Having achieved a well-posed eigenvalue problem, its solution will be used to unravel both the characteristic eigenmode frequencies and the eigensolutions corresponding to our principal variables, u_r, u_θ, u_z , and p .

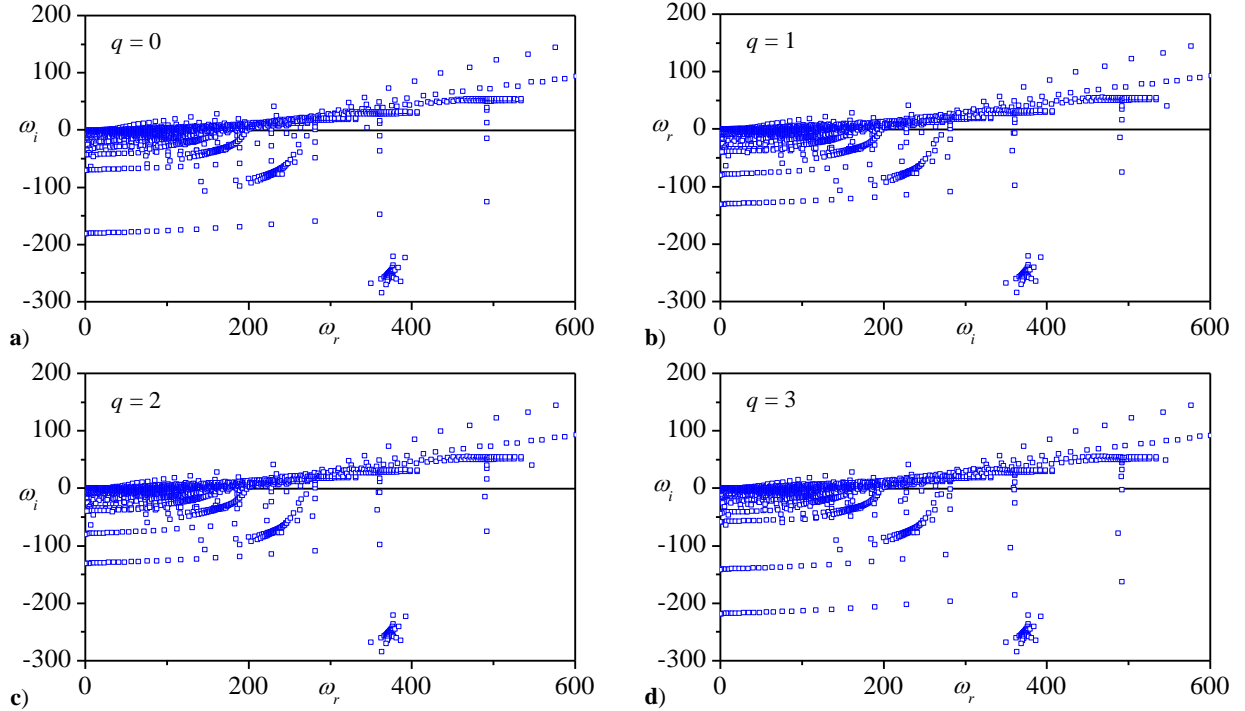


Figure 2. Spectral results for a solid rocket motor with $Re = 5 \times 10^3$, $u_h = 0$, and $q = 0, 1, 2$, and 3 in Parts a) through d).

V. Results and Discussion

A. Solid Rocket Motor with Inert Headwall

The first test case in this study considers a cylindrically-shaped SRM with a nonreactive headwall, i.e. $u_h = 0$. Figure 2 provides the eigensolutions for the simulated SRM with $Re = 5000$ and four azimuthal wave numbers evolving from 0 to 3. By increasing q , the spectral frequencies that fall within the unstable region, above the $\omega_i = 0$ horizontal line, seem to be quite similar in both trend and amplitude as they follow a rather linear behavior. Upon closer look, we find that the initial unstable frequencies for each q move closer to the $\omega_r = 0$ axis with successive increases in q . Also depicted in Figure 2 is the clustering of eigenmodes in the stable region, below the horizontal line. In the cluttered area, the linear trends that characterize the unstable eigenmodes cease to exist. Instead, the clustering seems to adhere to no particular order.

From Figure 2, the maximum circular frequency below which the flow becomes stable can be estimated. Using $Re = 5000$ and $u_h = 0$, the threshold frequencies are calculated to be $\omega_r = 25.32, 22.86, 25.82,$ and 14.06 for $q = 0, 1, 2,$ and 3 , respectively. To aid in visualizing the behavior of the first unstable eigensolution, a magnification of the spectrum is provided in Figure 3 for $q = 3$, where a red circle is used to pinpoint the mode in question. This particular eigenmode, $\omega = 14.054 + 0.0901i$, is further explored by evaluating its eigensolutions in Figure 4, where isocontours are provided for the radial, tangential, and axial velocities (Figure 4a,b,c). Our results indicate that moderate fluctuations in u_r can occur in the headwall region, whereas strong fluctuations in u_θ and u_z may be seen throughout the entire chamber. Fluctuations in the latter seem to faithfully follow the mean flow streamlines. Lastly, we show in Figure 4d the hydrodynamic pressure oscillations that develop in the flow. These seem to appear just as the axial oscillations begin to dissipate and slowly decrease in amplitude while approaching the exit plane at $z = Z_N$.

D. Solid Rocket Motor with Reactive Headwall

Based on the LNP investigation by Abu-Irshaid, Majdalani, and Casalis,³⁹ one is able to predict the stability breakdown region for a solid rocket motor that is subject to uniformly distributed propellant burning along both its sidewall and headwall. Thus using $Re = 5000$, $q = 0$, and $u_h = \frac{1}{2}$, the bulk flowfield is found to be stable below a dimensionless frequency of $\omega_r = 28.5$. For $q = 2$, the threshold frequency below which the flow stabilizes increases to $\omega_r = 34$. These results are reproduced in Figure 5 where the neutral curves and threshold frequencies predicted by the LNP approach are provided. Using identical conditions, the spectral results that we obtain using the biglobal framework are depicted in Figure 6. As one may infer from Figure 6b, our spectral analysis may be viewed as somewhat concurrent with the LNP approach: In lieu of $\omega_r = 28.5$, the present framework projects a threshold value of $\omega_r = 26.87$ for the first unstable eigenvalue at $q = 0$. The discrepancies between the LNP and biglobal stability outcomes may be partly attributed to the absence of outflow boundary conditions in the LNP approach. Furthermore, the LNP's specification of a longitudinal wave number may be viewed as being somewhat restrictive in the sense that it pre-establishes the periodic behavior of the solution in the streamwise direction. By comparison, the spatial behavior, which is implicitly captured in the biglobal approach, tends to be more realistic. Lastly, the application of the LNP approach to essentially nonparallel rocket flowfields can result in a finite error, unlike the biglobal approach.

In complementing this $q = 0$ test case, Figure 7 is used to display the spectra associated with $Re = 5000$, $u_h = \frac{1}{2}$, and two successive values of the tangential wave number, namely, $q = 1$ and 2 . Here too, a qualitative agreement may be drawn between the biglobal stability predictions and those of the LNP approach.³⁹ The threshold frequencies in this study are found to be $\omega_r = 28.76$ and 31.1 for $q = 1$ and 2 , respectively. Those deduced from the LNP approach return similar values of $\omega_r = 28.5$ and 34 , which fall within 1.8% and 9.3% of their biglobal stability counterparts, respectively.

Compared to the SRM configuration with inert headwall conditions (i.e. Figure 2), a similar behavior in wave frequencies and amplitudes is realized here. Specifically, spectral values in the unstable region do not appear to

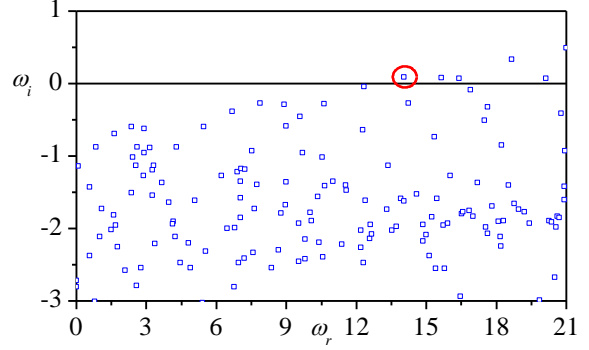


Figure 3. First unstable eigensolution for a solid rocket motor with $Re = 5 \times 10^3$, $u_h = 0$, and $q = 3$.

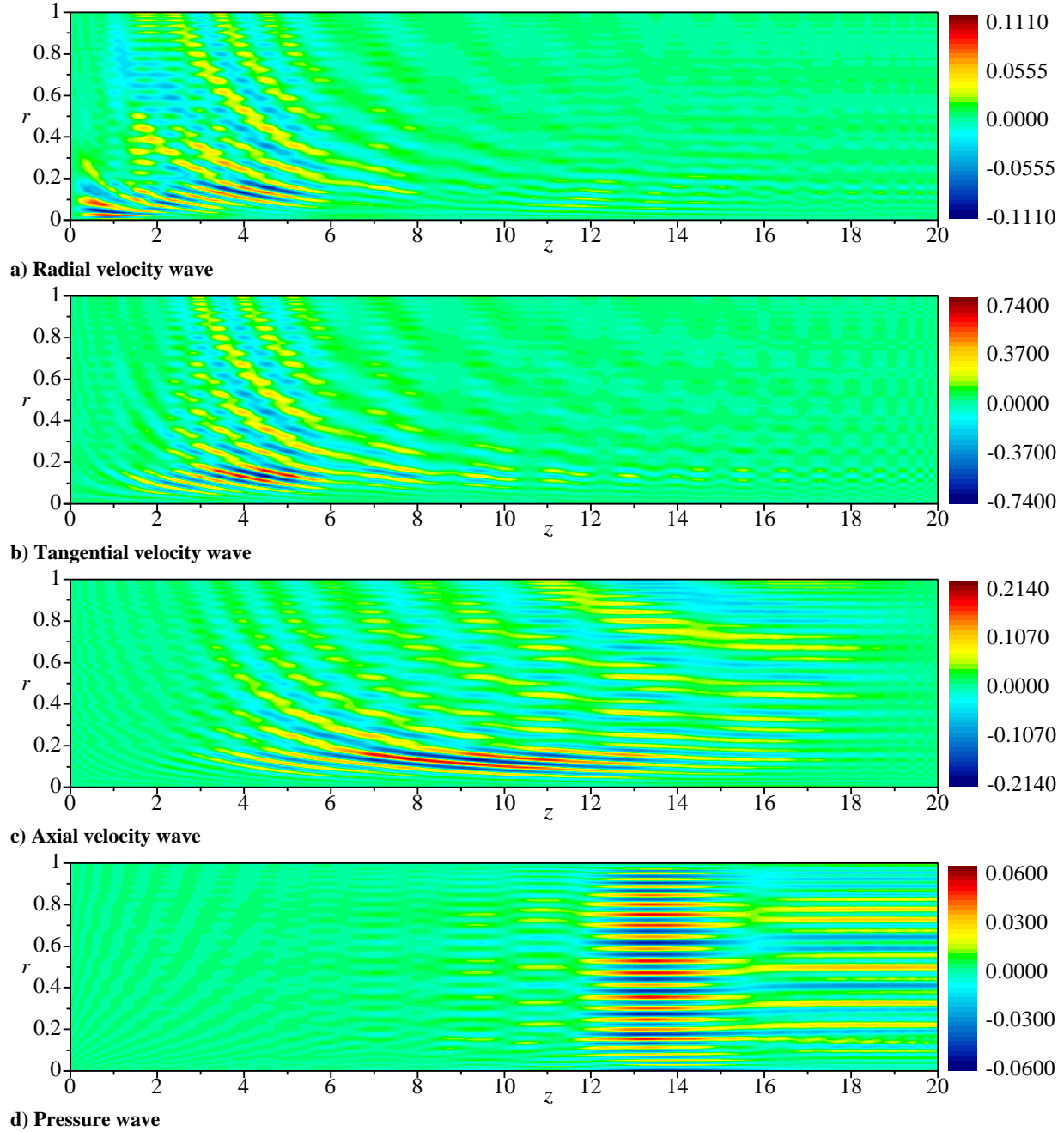


Figure 4. Eigensolutions for the first unstable eigenvalue $\omega_{31} = 14.06 + 0.0901i$ with $q = 3$, $Re = 5 \times 10^3$, and $u_h = 0$.

exhibit appreciable changes in either trend or amplitude. As before, the initial unstable eigenmodes for each wave number q tend to gravitate away from the vertical $\omega_r = 0$ axis as q is increased, thus extending the region of stability in a manner that is qualitatively consistent with the trends associated with the LNP approach.³⁹ Figure 7 also reflects the presence of mode clustering in the stable region, which clearly resembles the data scatter obtained for $u_h = 0$ in Figure 2. Moreover, the stable eigenmodes seem to progressively drop further and further below the horizontal stability axis as q is incremented. This downward shift confirms that the flow becomes fundamentally more stable at higher values of q .

At $q = 3$, the first two unstable modes retrieved through biglobal analysis correspond to $\omega_{31} = 26.06 + 0.2377i$ and $\omega_{32} = 27.61 + 0.5163i$, where ω_{qm} refers to the m^{th} eigenmode for a tangential wave number q . In this

situation, ω_{32} exhibits a higher temporal growth rate than ω_{31} . The eigensolutions associated with these two modes are depicted in Figures 8 and 9, respectively.

In Figure 8, it may be seen that the fluctuations in the radial velocity near the headwall are less pronounced than in the inert headwall case. This is due to the parallel flow inertia caused by axial injection at $z=0$, which suppresses the tendency of radial oscillations to grow in the headwall region. As for the tangential and axial velocity distributions, a strong agreement between the inert and reactive headwall cases may be seen, namely, in the form of appreciable disturbances that intensify as the centerline is approached. Here too, the disturbances seem to faithfully follow the steady-state streamline patterns in the chamber, with the highest amplitudes occurring in the region of maximum shear, i.e. where streamline curvatures tend to be the sharpest. Compared to the inert headwall case, the axial velocity fluctuations increase in magnitude due to the added headwall injection. The pressure oscillations also increase in magnitude compared to the case with no headwall injection. Their distribution seems to be nearly orthogonal to that of the velocity disturbances, with their largest magnitudes appearing in the region where the streamline curvatures start to flatten out.

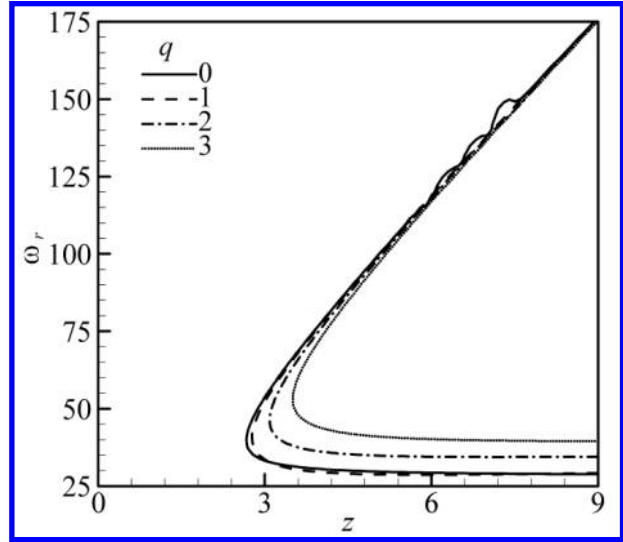


Figure 5. Neutral curves from the one-dimensional LNP approach³⁹ using $Re = 5 \times 10^3$ and $u_h = 0.5$.

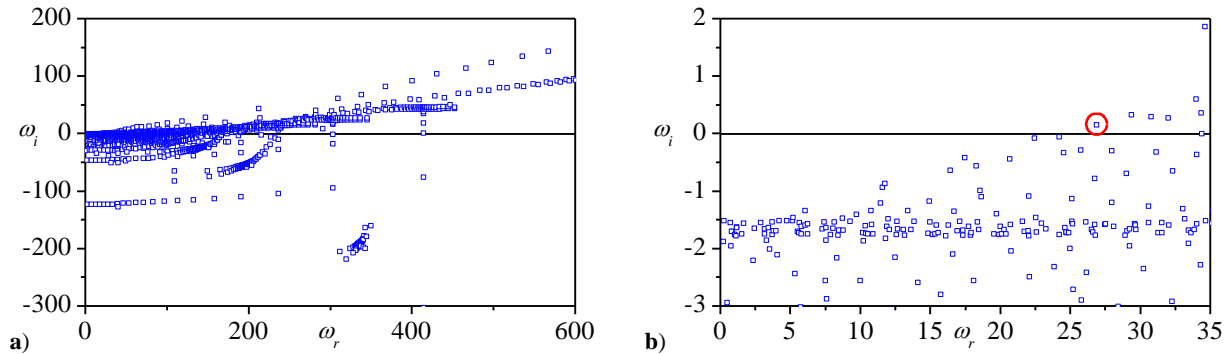


Figure 6. Spectral results of a solid rocket motor with $Re = 5 \times 10^3$, $u_h = 0.5$, and $q = 0$ showing a) the overall frequency spectrum and b) a magnification region where the first unstable eigenmode may be identified.

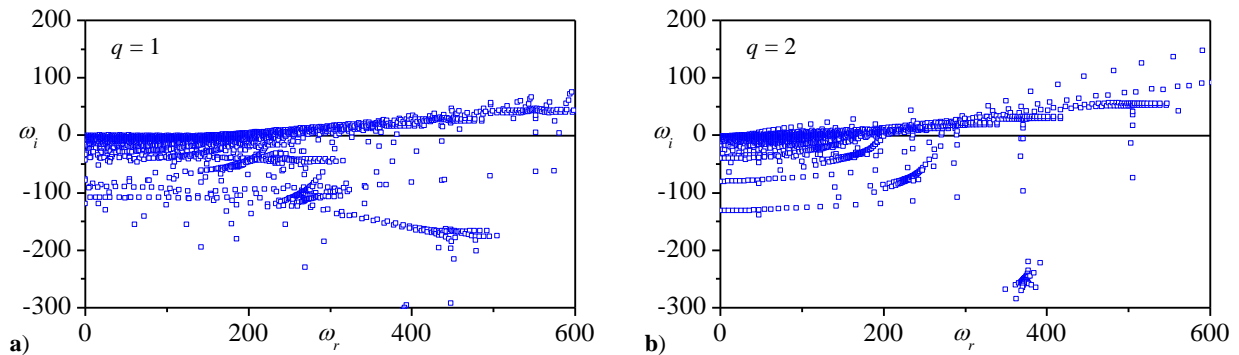


Figure 7. Spectral results for a solid rocket motor with $Re = 5 \times 10^3$ and $u_h = 0.5$ using a) $q = 1$ and b) 2.

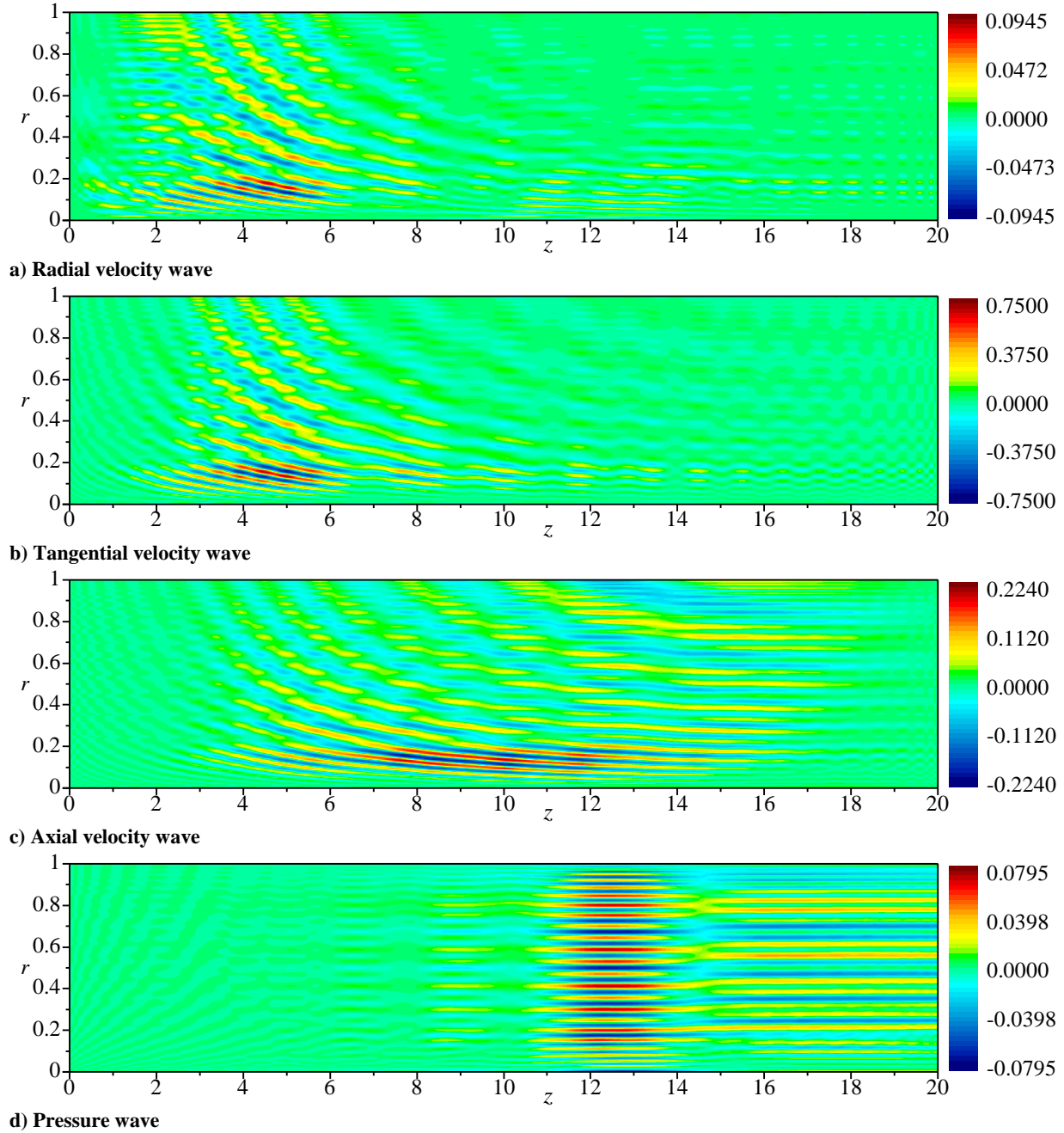


Figure 8. Eigensolutions for the first unstable eigenvalue $\omega_{31} = 26.07 + 0.2377i$ with $q = 3$, $Re = 5 \times 10^3$, and $u_h = 0.5$.

As we move to a more unstable eigenmode, we note that $(\omega_{32})_i > (\omega_{31})_i$. We therefore use Figure 9 to illustrate the contours of the perturbations in the radial, tangential, and axial waves for $\omega_{32} = 27.61 + 0.5163i$. Compared to the first unstable mode, we calculate $(\omega_{32})_i / (\omega_{31})_i \approx 0.5163 / 0.2377 \approx 2.17$. The frequency growth rate of the second mode proves to be more than twice its precursor, which is featured in Figure 8. At the outset, the large amplitude fluctuations in Figure 9 are seen to be more pervasive, thus extending over a larger portion of the chamber. For example, the high amplitude fluctuations in all components are manifested not only in the core region, but all the way to the chamber wall. This behavior is indicative that the flowfield is not only unstable in the core region, but throughout the entire chamber. Furthermore, the triggered oscillations seem to exhibit better resistance to dissipation while approaching the choked exit section. Unlike the first unstable mode, where velocity fluctuations are quickly suppressed in the downstream direction, the larger temporal growth rate of $(\omega_{32})_i$ leads to higher

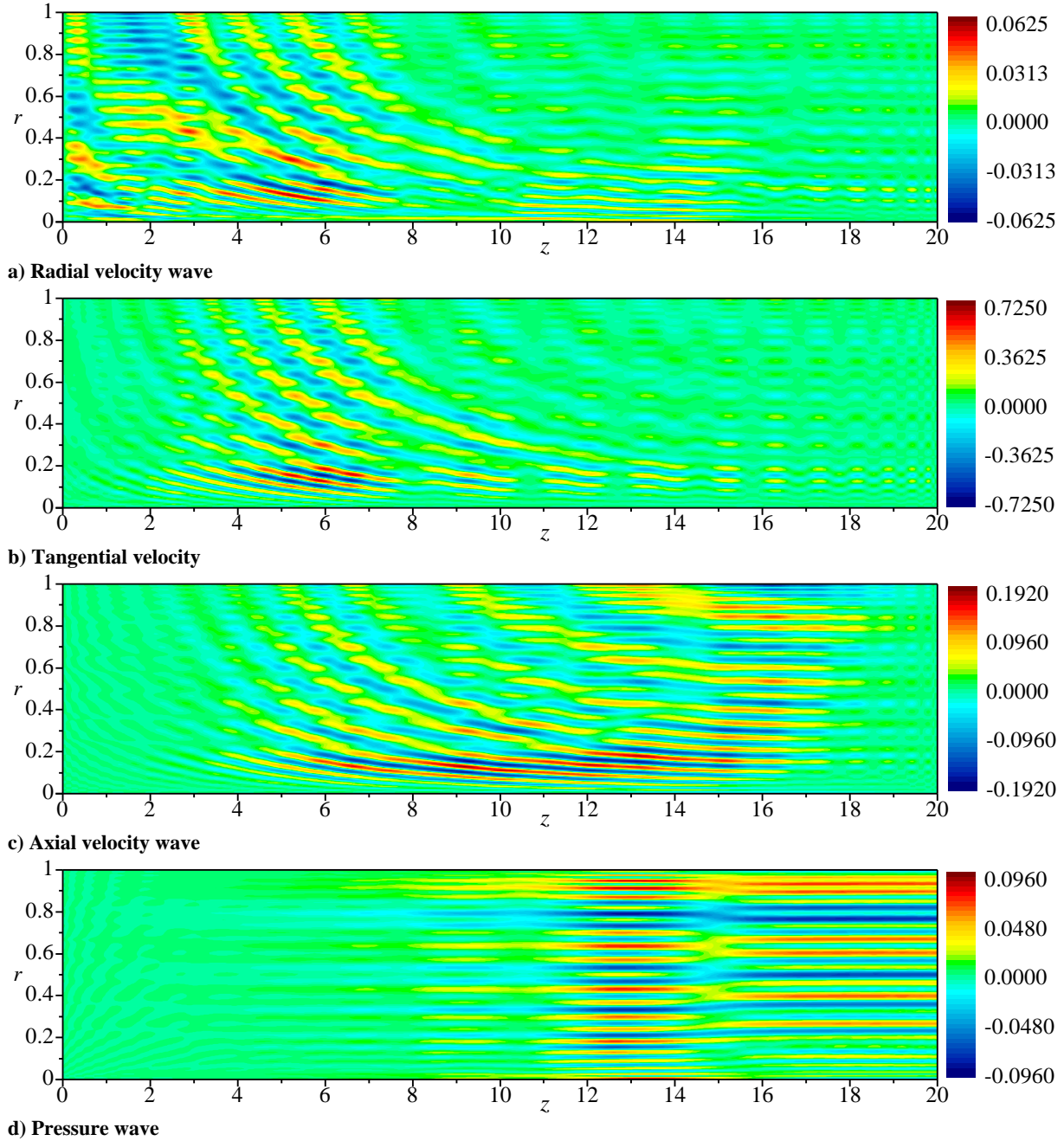


Figure 9. Eigensolutions for the second unstable eigenvalue $\omega_{32} = 27.61 + 0.5163i$ with $q = 3$, $Re = 5 \times 10^3$, and $u_h = 0.5$.

amplitudes in the vicinity of the exit plane. The increased ω_i also leads to more uniform amplitudes in the pressure fluctuations. As shown in Figure 9d, these seem to retain their magnitudes and spread across the chamber diameter while propagating axially.

E. Hybrid Rocket Engine

The final investigation is directed toward a hybrid rocket engine case with a headwall injection constant of $u_h = 50$. The spectrum for the hybrid rocket with a Reynolds number of 5000 and two azimuthal wave numbers of 0 and 3 are depicted in Figure 10. This graph features the first unstable eigenmodes for both cases of q . Based on the biglobal stability approach, we find that the first unstable eigenmodes at $q = 0$ and 3 yield $\omega_{01} = 21.95 + 2.523i$

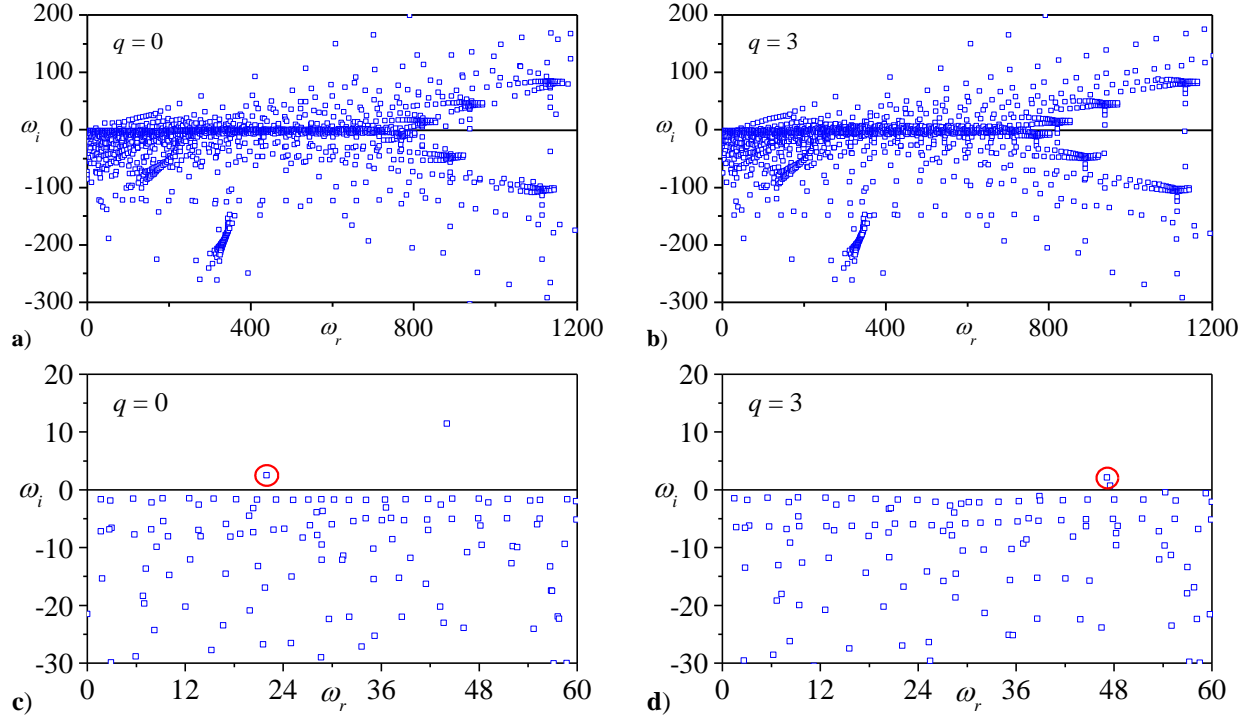


Figure 10. Spectral results for a hybrid rocket engine with $Re = 5 \times 10^3$ and $u_h = 50$ using a) $q = 0$ and b) 3. The magnifications in c) and d) serve to identify the first unstable eigenmodes for the two cases considered.

and $\omega_{31} = 47.13 + 2.15i$. After careful scrutiny, we realize that the changes in headwall injection, which correspond to realistic hybrid rocket configurations, correlate directly with the frequency growth. This correlation may be corroborated by comparing the spectral results obtained heretofore, namely, in Sections A through C. Accordingly, the unstable frequency seems to increase with u_h both in magnitude, with respect to its circular frequency, and in the number of unstable eigenmodes. Our results also suggest that a greater scatter is induced by successive increases in u_h . As depicted in Figure 10, an interesting pattern of modal distributions may be inferred from the resulting spectra irrespective of the azimuthal mode number. Going from $q = 0$ to 3, eigenmodes are seen to evolve into two families of rays that obliquely diverge from the stability axis, either upwardly or downwardly. The clustering of these modes along the neutral axis extends from a dimensionless frequency of $\omega_r = 0$ to approximately 800. Beyond this frequency, the bifurcation of eigenmodes ceases to originate along the neutral axis.

The first unstable eigenmode, $\omega_{31} = 47.13 + 2.15i$, which is pinpointed in Figure 10d, is further explored in Figure 11 through a display of its unsteady flowfield ingredients. In the case of a simulated hybrid, the streamtube motion that dominates throughout the chamber is evident. The parallel flow straightening caused by strong headwall injection is clearly conveyed to all fluctuating components. These appear to undulate about the mean flow streamlines, thus forming segmented regions that extend from the headwall to the exit plane. These segments are characterized by rather self-similar oscillations that start at the sidewall and expand in width as the centerline is approached. They also intensify and stretch horizontally as more mass is picked up with successive increases in z . Given that computed amplitudes are irrelevant in an eigenvalue problem (due to arbitrary scaling), what may be more important to identify than actual magnitudes is the frequency of occurrence of velocity extrema. In the case of a cylindrically-shaped hybrid engine, the peak values associated with the three velocity disturbances seem to occur more frequently than in the SRM case. Furthermore, by examining the fluctuations in the axial and tangential velocity components at a particular location in the chamber, especially near the centerline, one may infer that vorticity generation is increased compared to similarly unstable modes of SRMs with minimal or no headwall injection. As for the unsteady pressure contours that accompany this unstable mode, they tend to smoothly follow the streamtube motion, with their largest magnitudes occurring in an annular region extending between 10% and 50% of the chamber diameter (i.e. $0.1 < r < 0.5$).

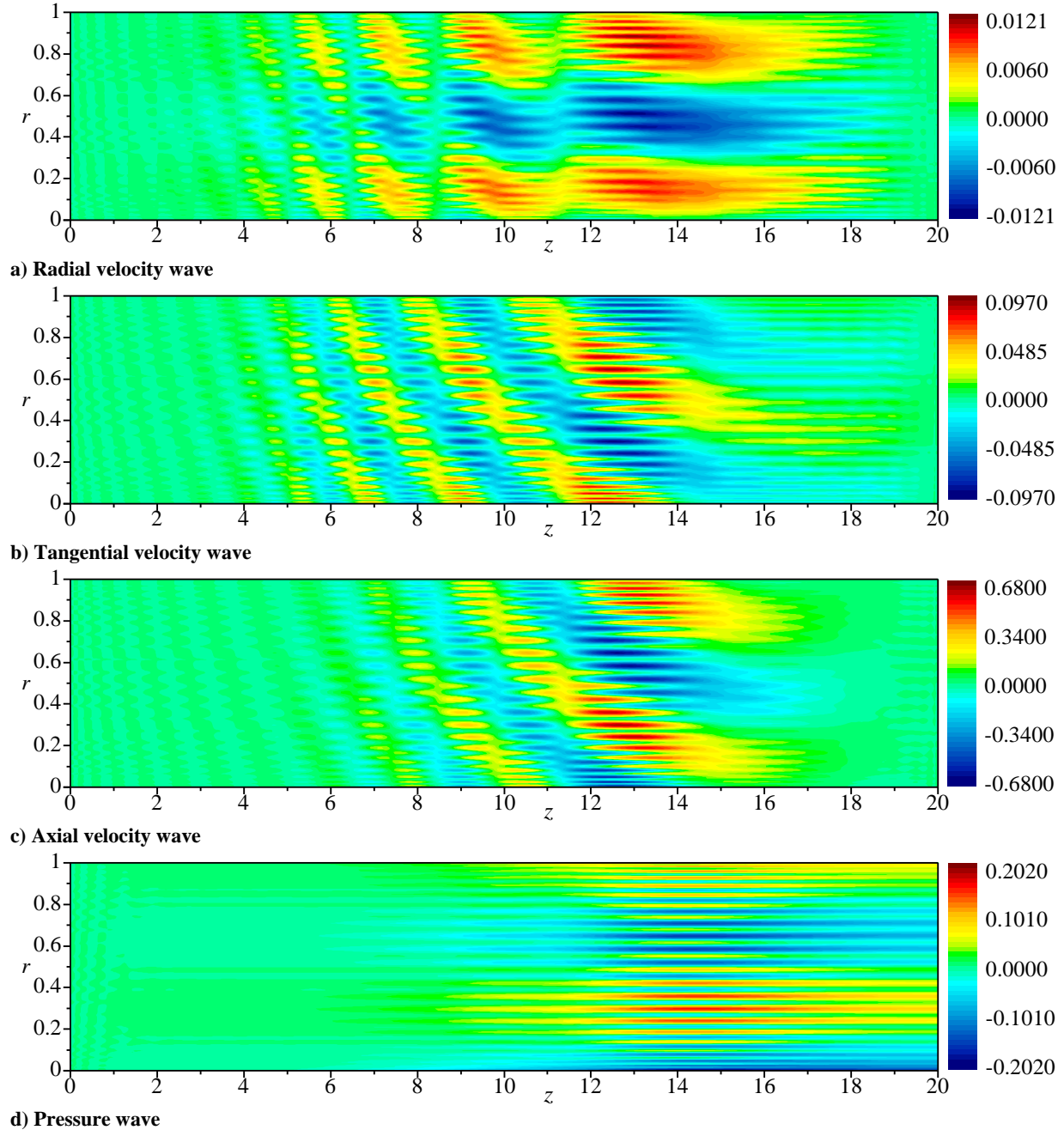


Figure 11. Eigensolutions for the first unstable eigenvalue $\omega_{31} = 47.1326 + 2.1496i$ with $q = 3$, $Re = 5 \times 10^3$, and $u_h = 50$.

For the reader's convenience, the streamlines associated with the extended Taylor-Culick profile⁴⁰ are illustrated in Figure 12 using $u_h = 50$ and a sufficiently large Reynolds number. This graph serves to illuminate the strong connection between the mean flow character and the generation and propagation of biglobal stability disturbances.

VI. Conclusions

In this paper, a biglobal stability framework is used to investigate the growth of disturbances in three idealized rocket chambers: a solid rocket with inert headwall, a solid rocket motor with a reactive headwall, and a hybrid rocket engine with sufficiently large headwall injection. Despite the increased accuracy associated with our two-dimensional approach, the spectral results that we obtain seem to compare favorably with those reported previously

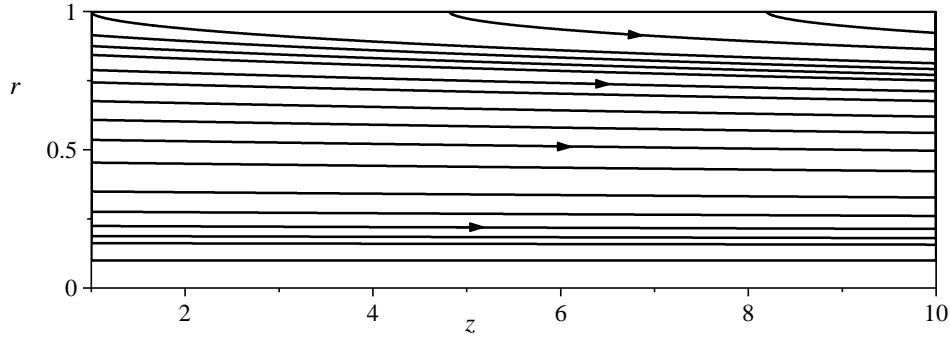


Figure 12. Mean flow streamlines illustrating the streamtube motion associated with the extended Taylor-Culick profile⁴⁰ which is used to model the bulk gaseous transport in a simulated hybrid rocket engine with $u_h = 50$.

using a one-dimensional formulation, namely, that of the Local Nonparallel (LNP) approach.³⁹ In the majority of cases modeled, our spectra seem to exhibit similar frequency thresholds to those acquired using a one-dimensional representation for the three systems under investigation. Overall, our results show that the range of unstable frequencies increases with successive increases in headwall injection, thus making a hybrid rocket flowfield more unstable than that of a solid rocket motor. Paradoxically, we also find that the first unstable eigenmode proves to be more sensitive to variations in the azimuthal wave number q than to changes in the headwall injection constant u_h . Finally, we find that as u_h is increased, the shift in ω_i with successive increases in ω_r also increases. However, a direct numerical correlation between these two parameters has yet to be determined.

In this work, the boundary conditions in the exit plane are chosen as though the engine is choked at $z = Z_N$, despite the underlying assumption of an incompressible fluid. It would be interesting to investigate the sensitivity of the eigenmodes to the length of the chamber Z_N . It would also be helpful to re-evaluate the eigenmodes using a different set of outflow conditions that correspond to an incompressible fluid with vanishing normal stresses in the exit plane. The relevance of such conditions is discussed by Casalis, Boyer and Radenac.⁵¹ These modifications will be considered in future work along with a wider parametric selection of test cases that will focus more closely on the hybrid rocket configuration.

Acknowledgments

This material is based on work supported partly by the National Science Foundation and partly by the University of Tennessee Space Institute.

References

- ¹Varapaev, V., and Yagodkin, V., "Flow Stability in a Channel with Porous Walls," *Fluid Dynamics (Izvestiya Akademii Nauk SSSR, Mechanika Zhidkosti i Gaza)*, Vol. 4, No. 5, 1969, pp. 91-95. doi: [10.1007/BF01015958](https://doi.org/10.1007/BF01015958)
- ²Beddini, R. A., "Injection-Induced Flows in Porous-Walled Ducts," *AIAA Journal*, Vol. 24, No. 11, 1986, pp. 1766-1773. doi: [10.2514/3.9522](https://doi.org/10.2514/3.9522)
- ³Beddini, R. A., and Roberts, T. A., "Turbularization of an Acoustic Boundary Layer on a Transpiring Surface," *AIAA Journal*, Vol. 26, No. 8, 1988, pp. 917-923. doi: [10.2514/3.9991](https://doi.org/10.2514/3.9991)
- ⁴Lee, Y., and Beddini, R. A., "Acoustically-Induced Turbulent Transition in Solid Propellant Rocket Chamber Flowfields," AIAA Paper 99-2508, June 1999.
- ⁵Lee, Y., and Beddini, R. A., "Effect of Solid Rocket Chamber Pressure on Acoustically-Induced Turbulent Transition," AIAA Paper 2000-3802, July 2000.
- ⁶Apte, S., and Yang, V., "Effect of Acoustic Oscillation on Flow Development in a Simulated Nozzleless Rocket Motor," *Solid Propellant Chemistry, Combustion, and Motor Interior Ballistics*, Vol. 185, edited by V. Yang, T. B. Brill, and W.-Z. Ren, AIAA Progress in Astronautics and Aeronautics, Washington, DC, 2000, pp. 791-822.
- ⁷Apte, S., and Yang, V., "Unsteady Flow Evolution in a Porous Chamber with Surface Mass Injection. Part I: Free Oscillation," *AIAA Journal*, Vol. 39, No. 8, 2001, pp. 1577-1586. doi: [10.2514/2.1483](https://doi.org/10.2514/2.1483)
- ⁸Apte, S., and Yang, V., "Unsteady Flow Evolution in a Porous Chamber with Surface Mass Injection. Part II: Acoustic Excitation," *AIAA Journal*, Vol. 40, No. 2, 2002, pp. 244-253. doi: [10.2514/2.1666](https://doi.org/10.2514/2.1666)
- ⁹Wasistho, B., Balachandar, S., and Moser, R., "Compressible Wall-Injection Flows in Laminar, Transitional, and Turbulent Regimes: Numerical Prediction," *Journal of Spacecraft and Rockets*, Vol. 41, No. 6, 2004, pp. 915-924. doi: [10.2514/1.2019](https://doi.org/10.2514/1.2019)
- ¹⁰Casalis, G., Avalon, G., and Pineau, J.-P., "Spatial Instability of Planar Channel Flow with Fluid Injection through Porous Walls," *Physics of Fluids*, Vol. 10, No. 10, 1998, pp. 2558-2568. doi: [10.1063/1.869770](https://doi.org/10.1063/1.869770)

- ¹¹Griffond, J., Casalis, G., and Pineau, J., "Spatial Instability of Flow in a Semiinfinite Cylinder with Fluid Injection through Its Porous Walls," *European Journal of Mechanics B/Fluids*, Vol. 19, No. 1, 2000, pp. 69-87. doi: [10.1016/S0997-7546\(00\)00105-9](https://doi.org/10.1016/S0997-7546(00)00105-9)
- ¹²Ugurtas, B., Avalon, G., Lupoglazoff, N., Vuillot, F., and Casalis, G., "Stability and Acoustic Resonance of Internal Flows Generated by Side Injection," *Solid Propellant Chemistry, Combustion, and Motor Interior Ballistics*, Vol. 185, edited by V. Yang, T. B. Brill, and W.-Z. Ren, AIAA Progress in Astronautics and Aeronautics, Washington, DC, 2000, pp. 823-836.
- ¹³Griffond, J., and Casalis, G., "On the Dependence on the Formulation of Some Nonparallel Stability Approaches Applied to the Taylor Flow," *Physics of Fluids*, Vol. 12, No. 2, 2000, pp. 466-468. doi: [10.1063/1.870323](https://doi.org/10.1063/1.870323)
- ¹⁴Griffond, J., and Casalis, G., "On the Nonparallel Stability of the Injection Induced Two-Dimensional Taylor Flow," *Physics of Fluids*, Vol. 13, No. 6, 2001, pp. 1635-1644. doi: [10.1063/1.1367869](https://doi.org/10.1063/1.1367869)
- ¹⁵Férraille, T., and Casalis, G., "Channel Flow Induced by Wall Injection of Fluid and Particles," *Physics of Fluids*, Vol. 15, No. 2, 2003, pp. 348-360. doi: [10.1063/1.1530158](https://doi.org/10.1063/1.1530158)
- ¹⁶Fabignon, Y., Dupays, J., Avalon, G., Vuillot, F., Lupoglazoff, N., Casalis, G., and Prévost, M., "Instabilities and Pressure Oscillations in Solid Rocket Motors," *Journal of Aerospace Science and Technology*, Vol. 7, No. 3, 2003, pp. 191-200. doi: [10.1016/S1270-9638\(02\)01194-X](https://doi.org/10.1016/S1270-9638(02)01194-X)
- ¹⁷Prévost, M., Godon, J., and Innegraeve, O., "Thrust Oscillations in Reduced Scale Solid Rocket Motors, Part I : Experimental Investigations," AIAA Paper 2005-4003, July 2005.
- ¹⁸Avalon, G., Casalis, G., and Griffond, J., "Flow Instabilities and Acoustic Resonance of Channels with Wall Injection," AIAA Paper 98-3218, July 1998.
- ¹⁹Avalon, G., and Comas, P., "Simulative Study of the Unsteady Flow inside a Solid Propellant Rocket Motor," AIAA Paper 91-1866, June 1991.
- ²⁰Vuillot, F., and Avalon, G., "Acoustic Boundary Layers in Large Solid Propellant Rocket Motors Using Navier-Stokes Equations," *Journal of Propulsion and Power*, Vol. 7, No. 2, 1991, pp. 231-239. doi: [10.2514/3.23316](https://doi.org/10.2514/3.23316)
- ²¹Vuillot, F., "Vortex-Shedding Phenomena in Solid Rocket Motors," *Journal of Propulsion and Power*, Vol. 11, No. 4, 1995, pp. 626-639. doi: [10.2514/3.23888](https://doi.org/10.2514/3.23888)
- ²²Couton, D., Doan-Kim, S., and Vuillot, F., "Numerical Simulation of Vortex-Shedding Phenomenon in a Channel with Flow Induced through Porous Wall," *International Journal of Heat and Fluid Flow*, Vol. 18, No. 3, 1997, pp. 283-296. doi: [10.1016/S0142-727X\(97\)00005-2](https://doi.org/10.1016/S0142-727X(97)00005-2)
- ²³Ugurtas, B., Avalon, G., Lupoglazoff, N., and Vuillot, F., "Numerical Computations of Hydrodynamic Instabilities inside Channels with Wall Injection," AIAA Paper 99-2505, June 1999.
- ²⁴Chedeveigne, F., and Casalis, G., "Thrust Oscillations in Reduced Scale Solid Rocket Motors, Part II : A New Theoretical Approach," AIAA Paper 2005-4000, July 2005.
- ²⁵Chedeveigne, F., and Casalis, G., "Detailed Analysis of the Thrust Oscillations in Reduced Scale Solid Rocket Motors," AIAA Paper 2006-4424, July 2006.
- ²⁶Chedeveigne, F., Casalis, G., and Férraille, T., "Biglobal Linear Stability Analysis of the Flow Induced by Wall Injection," *Physics of Fluids*, Vol. 18, No. 1, 2006, pp. 014103-14. doi: [10.1063/1.2160524](https://doi.org/10.1063/1.2160524)
- ²⁷Chedeveigne, F., Casalis, G., and Majdalani, J., "Direct Numerical Simulation and Biglobal Stability Investigations of the Gaseous Motion in Solid Rocket Motors," *Journal of Fluid Mechanics*, Vol. FirstView (online), 2012, pp. 1-29. doi: [10.1017/jfm.2012.245](https://doi.org/10.1017/jfm.2012.245)
- ²⁸Majdalani, J., and Van Moorhem, W., "Improved Time-Dependent Flowfield Solution for Solid Rocket Motors," *AIAA Journal*, Vol. 36, No. 2, 1998, pp. 241-248. doi: [10.2514/2.7507](https://doi.org/10.2514/2.7507)
- ²⁹Batterson, J. W., and Majdalani, J., "Biglobal Instability of the Bidirectional Vortex. Part 1: Formulation," AIAA Paper 2011-5648, July-August 2011.
- ³⁰Batterson, J. W., and Majdalani, J., "Biglobal Instability of the Bidirectional Vortex. Part 2: Complex Lamellar and Beltrami Motions," AIAA Paper 2011-5649, July-August 2011.
- ³¹Chiaverini, M. J., Malecki, M. J., Sauer, J. A., Knuth, W. H., and Hall, C. D., "Final Report on Cold-Wall Vortex Combustion Chamber – a Phase I SBIR Project," Orbital Technologies Corporation, NASA Contact No. NAS8-01073 Rept. OTC-GS0107-01-1, Madison, Wisconsin, August, 2001.
- ³²Chiaverini, M. J., Malecki, M. M., Sauer, J. A., Knuth, W. H., and Hall, C. D., "Testing and Evaluation of Vortex Combustion Chamber for Liquid Rocket Engines," JANNAF Paper TP-2002-0372, April 2002.
- ³³Sauer, J. A., Malecki, M. M., Knuth, W. H., Chiaverini, M. J., and Hall, C. D., "Development of a LOX/RP-1 Vortex Combustion Cold-Wall Thrust Chamber Assembly," AIAA Paper 2002-4144, July 2002.
- ³⁴Chiaverini, M. J., Malecki, M. J., Sauer, J. A., Knuth, W. H., and Majdalani, J., "Vortex Thrust Chamber Testing and Analysis for O₂-H₂ Propulsion Applications," AIAA Paper 2003-4473, July 2003.
- ³⁵Majdalani, J., and Chiaverini, M. J., "On Steady Rotational Cyclonic Flows: The Viscous Bidirectional Vortex," *Physics of Fluids*, Vol. 21, No. 10, 2009, pp. 103603-15. doi: [10.1063/1.3247186](https://doi.org/10.1063/1.3247186)
- ³⁶Batterson, J. W., and Majdalani, J., "Sidewall Boundary Layers of the Bidirectional Vortex," *Journal of Propulsion and Power*, Vol. 26, No. 1, 2010, pp. 102-112. doi: [10.2514/1.40442](https://doi.org/10.2514/1.40442)
- ³⁷Batterson, J. W., and Majdalani, J., "On the Viscous Bidirectional Vortex. Part 1: Linear Beltrami Motion," AIAA Paper 2010-6763, July 2010.
- ³⁸Batterson, J. W., and Majdalani, J., "On the Viscous Bidirectional Vortex. Part 2: Nonlinear Beltrami Motion," AIAA Paper 2010-6764, July 2010.

- ³⁹Abu-Irshaid, E. M., Majdalani, J., and Casalis, G., "Hydrodynamic Stability of Rockets with Headwall Injection," *Physics of Fluids*, Vol. 19, No. 2, 2007, pp. 024101-11. [doi: 10.1063/1.2434797](https://doi.org/10.1063/1.2434797)
- ⁴⁰Majdalani, J., "Analytical Models for Hybrid Rockets," *Fundamentals of Hybrid Rocket Combustion and Propulsion*, edited by K. Kuo and M. J. Chiaverini, AIAA Progress in Astronautics and Aeronautics, Washington, DC, 2007, pp. 207-246.
- ⁴¹Majdalani, J., and Akiki, M., "Rotational and Quasiviscous Cold Flow Models for Axisymmetric Hybrid Propellant Chambers," *Journal of Fluids Engineering*, Vol. 132, No. 10, 2010, pp. 101202-7. [doi: 10.1115/1.4002397](https://doi.org/10.1115/1.4002397)
- ⁴²Majdalani, J., and Roh, T., "The Oscillatory Channel Flow with Large Wall Injection," *Proceedings of the Royal Society of London, Series A*, Vol. 456, No. 1999, 2000, pp. 1625-1657. [doi: 10.1098/rspa.2000.0579](https://doi.org/10.1098/rspa.2000.0579)
- ⁴³Majdalani, J., "Vorticity Dynamics in Isobarically Closed Porous Channels. Part I: Standard Perturbations," *Journal of Propulsion and Power*, Vol. 17, No. 2, 2001, pp. 355-362. [doi: 10.2514/2.5749](https://doi.org/10.2514/2.5749)
- ⁴⁴Majdalani, J., and Roh, T., "Vorticity Dynamics in Isobarically Closed Porous Channels. Part II: Space-Reductive Perturbations," *Journal of Propulsion and Power*, Vol. 17, No. 2, 2001, pp. 363-370. [doi: 10.2514/2.5750](https://doi.org/10.2514/2.5750)
- ⁴⁵Majdalani, J., "The Oscillatory Channel Flow with Arbitrary Wall Injection," *Journal of Applied Mathematics and Physics (ZAMP)*, Vol. 52, No. 1, 2001, pp. 33-61. [doi: 10.1007/PL00001539](https://doi.org/10.1007/PL00001539)
- ⁴⁶Majdalani, J., and Flandro, G., "The Oscillatory Pipe Flow with Arbitrary Wall Injection," *Proceedings of the Royal Society of London, Series A*, Vol. 458, No. 2023, 2002, pp. 1621-1651. [doi: 10.1098/rspa.2001.0930](https://doi.org/10.1098/rspa.2001.0930)
- ⁴⁷Robitaillie-Montané, C., and Casalis, G., "Méthode de Collocation Spectrale Appliquée à un Problème de Stabilité Donnée sous Forme d'Équations aux Dérivées Partielles," ONERA, Aerodynamics and Energetics Modeling (DMAE), Technical Rept., Toulouse, France, 2003.
- ⁴⁸Quarteroni, A., Sacco, R., and Saleri, F., *Numerical Mathematics*, edited by J. E. Marsden, L. Sirovich, M. Golubitsky, and Jäger, Springer Verlag, New York, 2007.
- ⁴⁹Voigt, R. G., Gottlieb, D., and Hussaini, M. Y., *Spectral Methods for Partial Differential Equations*, Society for Industrial and Applied Mathematics, 1984.
- ⁵⁰Trefethen, L. N., *Spectral Methods in Matlab*, Society for Industrial Mathematics, Oxford, 2000.
- ⁵¹Casalis, G., Boyer, G., and Radenac, E., "Some Recent Advances in the Instabilities Occurring in Long Solid Rocket Motors," AIAA Paper 2011-5642, July-August 2011.